Study of the L–I–H transition with a new dual gas puff imaging system in the EAST superconducting tokamak

2014 Nucl. Fusion 54 013007

(http://iopscience.iop.org/0029-5515/54/1/013007)

IOP Publishing | International Atomic Energy Agency Nuclear Fusion
Nucl. Fusion **54** (2014) 013007 (15pp) doi:10.1088/0029-5515/54/1/013007

Study of the L–I–H transition with a new dual gas puff imaging system in the EAST superconducting tokamak

G.S. Xu[1,7], L.M. Shao[1], S.C. Liu[1], H.Q. Wang[1], B.N. Wan[1], H.Y. Guo[1], P.H. Diamond[2,3], G.R. Tynan[2], M. Xu[4], S.J. Zweben[5], V. Naulin[6], A.H. Nielsen[6], J. Juul Rasmussen[6], N. Fedorczak[2], P. Manz[2], K. Miki[3], N. Yan[1,6], R. Chen[1], B. Cao[1], L. Chen[1], L. Wang[1], W. Zhang[1] and X.Z. Gong[1]

[1] Institute of Plasma Physics, Chinese Academy of Sciences, Hefei 230031, People's Republic of China
[2] CMTFO, University of California, San Diego, 9500 Gilman Drive, La Jolla, CA 92093, USA
[3] WCI Center for Fusion Theory, NFRI, Daejeon 305-333, Korea
[4] Southwestern Institute of Physics, PO Box 432, Chengdu 610041, People's Republic of China
[5] Princeton Plasma Physics Laboratory, Princeton, NJ 08540, USA
[6] Association Euratom-Risø DTU, DK-4000 Roskilde, Denmark

E-mail: gsxu@ipp.ac.cn

Received 1 March 2013, revised 13 October 2013
Accepted for publication 15 November 2013
Published 11 December 2013

Abstract

The intermediate oscillatory phase during the L–H transition, termed the I-phase, is studied in the EAST superconducting tokamak using a newly developed dual gas puff imaging (GPI) system near the L–H transition power threshold. The experimental observations suggest that the oscillatory behaviour appearing at the L–H transition could be induced by the synergistic effect of the two components of the sheared $m, n = 0$ $\boldsymbol{E} \times \boldsymbol{B}$ flow, i.e. the turbulence-driven zonal flow (ZF) and the equilibrium flow. The latter arises from the equilibrium, and is, to leading order, balanced by the ion diamagnetic term in the radial force balance equation. A slow increase in the poloidal flow and its shear at the plasma edge are observed tens of milliseconds prior to the I-phase. During the I-phase, the turbulence recovery appears to originate from the vicinity of the separatrix with clear wave fronts propagating both outwards into the far scrape-off layer (SOL) and inwards into the core plasma. The turbulence Reynolds stress is directly measured using the GPI system during the I-phase, providing direct evidence of kinetic energy transfer from turbulence to ZFs at the plasma edge. The GPI observations strongly suggest that the SOL transport physics and the evolution of pressure gradient near the separatrix play an important role in the L–I–H transition dynamics. To highlight these new physics, the previous predator–prey model is extended to include a new equation for the SOL physics. The model successfully reproduces the L–I–H transition process with several features comparing favourably with GPI observations.

Keywords: L–H transition, gas puff imaging, tokamak, zonal flow

1. Introduction

The L–H transition usually occurs very fast with a single-step sharp reduction of the fluctuation level on the time scale of tens of microseconds when the input heating power is well above the transition threshold or during a fast power ramp-up. However, as the input heating power is close to the transition threshold, an intermediate phase, the so-called 'I-phase' [1] or 'limit cycle oscillation' (LCO) [2], appears prior to the final transition into the H-mode. The associated L–H transition is previously termed as a 'dithering transition', or recently an 'L–I–H transition'. This phenomenon was first observed in JFT-2M [2, 3], and was also seen in AUG [4] referred to as 'dithering H-mode', JET [5], TEXTOR with electrode biasing [6], DIII-D [7, 8], H-1 stellarator [9] and W7-AS stellarator [10]. The number of cycles appearing during the transition increases with a decreasing ramping rate of the input heating power [4]. The I-phase is thought to provide a good opportunity for the study of causality in the transition physics.

Recently, there has been renewed interest in the L–H transition physics near the transition power threshold,

[7] Author to whom any correspondence should be addressed.

especially the dynamics of LCO [11–25], stimulated by the ITER requirement for H-mode operation in the initial non-active phases with limited power available [26], as well as remarkable progress in high-resolution diagnostic capability at the plasma edge that allows us to gain deeper insights into the physics of the L–H transition. These efforts start from the experiments in TJ-II stellarator [11] and NSTX [12], using a reflectometer and gas puff imaging (GPI), respectively, followed by experiments in AUG using a Doppler reflectometer showing LCO generated by the geodesic acoustic mode (GAM) modulation [1]. However, GAMs are observed to decrease in amplitude or are absent in several machines as the transition threshold conditions are approached, e.g. DIII-D [27, 28] and HL-2A [29]. Evidence for the low-frequency zonal flows (ZFs) playing a role in the LCO dynamics was obtained in EAST using toroidally separated two reciprocating probes [13]. It was found that periodic turbulence suppression occurs when the radial electric field (E_r) shearing rate transiently exceeds the turbulence decorrelation rate at the plasma edge. The spatiotemporal structure of the LCO was studied in TJ-II [14] and DIII-D [16] using a Doppler reflectometer, in NSTX [15] and C-Mod [17] using GPI. Evidence for triggering an L–H transition by ZFs with a sufficient strong Reynolds stress was obtained in EAST using a probe array [18]. Furthermore, an unexpected LCO similar to that preceding the L–H transition was observed following the L–H transition at marginal power in EAST [19]. Experimental results providing strong support for the predator–prey model of the ZF-driven LCO [30] have been obtained recently in DIII-D using probe measurements [22].

More recently, contradictory results have been reported [23–25]. Probe measurements in HL-2A show the existence of another kind of LCO [24] with opposite time sequences with respect to the ZF-driven LCO (normal LCO) [30] in addition to the normal LCO. The transition from the I-phase to the H-mode occurs only from the opposite LCO; however, the normal LCO is always observed in the L–I–L transition, i.e. a transition from L-mode via an I-phase, then back to L-mode. Such an opposite LCO has also been found recently in JFT-2M based on the analysis of the heavy ion beam probe (HIBP) data [25], where the Reynolds stress is found to be too small to accelerate the LCO flow. In addition, it is noted that the time sequences in the DIII-D experiments [16] are consistent with the opposite LCO instead of the normal LCO. It is currently thought that the opposite LCO may not be interpreted in terms of the ZFs. The diamagnetic component of the $E \times B$ flow is proposed to be the drive for the opposite LCO. However, questions still exist. The diamagnetic component of the $E \times B$ flow will principally introduce a positive feedback, which is unlikely to close a cycle without involving other feedback loops.

The first theory for the LCO was based on the bifurcation of the edge E_r and transport [2]. Then, Zohm showed that the LCO can be interpreted by a simple transport bifurcation model [4]. In recent years, ZFs and its capability of turbulence regulation have drawn significant attention [31, 32]. A model for the LCO based on a predator–prey interaction between the edge turbulence and the turbulence-driven ZFs was proposed [30]. This model was supported by several early experiments [7–9]. In this model, the ZFs introduce a feedback loop so that the cycle can be closed. The final transition into the H-mode is controlled by the 'mean flow' (MF) or sometimes termed 'equilibrium flow' (EF). The ZF and EF are the two components of the total $m, n = 0$ $\boldsymbol{E} \times \boldsymbol{B}$ flow, which is the leading order perpendicular guiding-centre flow, with the former being the time-varying component with mesoscale radial structures, driven by the radial gradient of turbulence Reynolds stress [33], and the latter arising from the equilibrium, to leading order, balanced by the ion diamagnetic term ($\partial_r p_\mathrm{i}/Z_\mathrm{i} e n_\mathrm{i} B$) in the radial force balance equation [34, 35]. Here, n and m are the toroidal and poloidal mode numbers, respectively. More recently, the ZF-driven LCO model [30] has been extended from zero dimensional (0D) to one dimensional (1D) in space [20, 21], showing that the LCO appears as a nonlinear wave originating from the separatrix, propagating inwards.

Currently, some debates on the role of ZF as a trigger for the L–H transition still exist. One should be aware that the energy transfer from turbulence to ZFs is not the only way for turbulence suppression. Turbulence level can be reduced by the well-known shear decorrelation mechanism [36, 37], which may directly reduce the effective growth rate of the underlying instability of turbulence. The shear decorrelation mechanism was revisited in a recent paper [38]. Physically, the shear decorrelation happens because the flow shear increases the effective wave number of the fluctuations in the direction along the shear [39], i.e. perpendicular to the flow, which scatters the turbulence spectral power into high-k regions where the dissipation dominates (because the dissipation goes with k^2) [38]. Here k stands for the wavenumber.

In parallel, significant efforts have been devoted recently to the study of the conditions and parameter dependence for the L–H transition power threshold [40–51], and dynamics for the L–H and H–L back transitions [52, 53].

The LCO has been studied previously in the 2010 experimental campaign on EAST using toroidally separated two reciprocating probes [13, 18, 19]. EAST is a fully superconducting tokamak with a modern divertor configuration [54]. To continue our previous work, in the 2012 campaign, a new dual GPI system with two viewing areas separated toroidally and poloidally [55] was constructed on EAST to provide direct measurements of the spatiotemporal evolution of the turbulence–flow oscillation pattern and turbulence Reynolds stress at the plasma edge during the I-phase. With this new diagnostic, the time-resolved poloidal and radial plasma flows at two well-separated locations can be obtained simultaneously by tracking the fast motion of turbulence structures in the plane perpendicular to the local magnetic field lines [56], thus allowing the $m, n = 0$ nature, i.e. poloidal and toroidal symmetry, of the ZF to be identified, as done previously with probes [13, 19, 57, 58] or HIBPs [59].

In the 2012 campaign, LCOs at a frequency from a few hundred Hz to several kHz appeared frequently near the transition threshold conditions in EAST. There were more than 1000 shots with L–I–H transitions in that campaign. The L–I–H transition was observed mostly in double-null (DN) or biased double-null configurations. There are only a few shots in single-null configurations with unfavourable $B \times \nabla B$ drift, i.e. away from the X-point, corresponding to the lower single-null (LSN) configuration, since the B_t in EAST is normally operated in the counter clockwise direction viewing from the

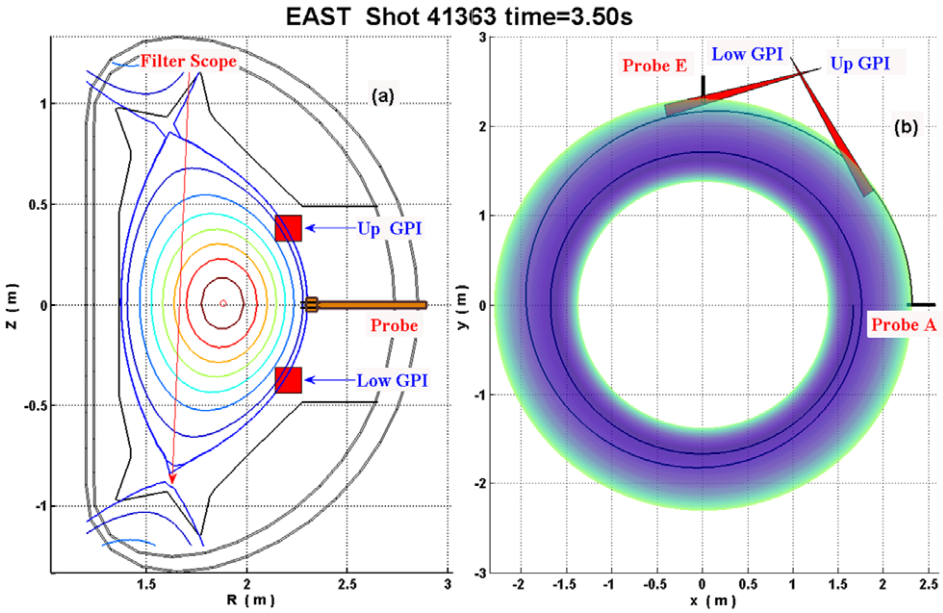

Figure 1. Illustration of the location of the new dual GPI diagnostic system, along with the two midplane reciprocating probe systems and the sightline of the filter scope system on EAST. (*a*) Cross-sectional view of the two imaging objective areas, up–down symmetrical about the midplane, separated poloidally by ∼100° around the magnetic axis. (*b*) Top view of the two GPI sightlines with two gas-cloud objective plane separated toroidally by 66.6°.

top. The mechanism for the configuration dependence is still unknown. It may have some connection to the 'I-mode' in C-Mod [60] and ASDEX-Upgrade [61], where the L–H transition threshold power is significantly higher with the unfavourable $B \times \nabla B$ direction. In addition, the L–I–H transitions were sometimes also observed when the power was considerably above, but still within a factor of 1.5 of the threshold; however, the L–I–L transitions were only seen when the power was very marginal to the threshold. The radiation power has been subtracted when we calculate the threshold power. The physical reason for the observation of the I-phase at excess L–H threshold power is still unclear. Some 'hidden variables' such as recycling or divertor pumping capability can significantly influence the power threshold.

The rest of this paper is organized as follows. In the following section, a brief introduction of the GPI diagnostic on EAST is given. In section 3, the GPI measurements of an L–I–H transition are described. In section 4, a self-consistent 0D model of the L–I–H transition is described, with comparisons made between modelling and experiments. A summary of the key points is given in section 5, along with conclusions and suggestions for further work.

2. GPI system on EAST

The GPI diagnostic is a measuring technique for imaging the local two-dimensional (2D) structure and fast motion of the edge plasma turbulence in the plane perpendicular to the local magnetic field lines [62]. A paper with detailed description of the new dual GPI system on EAST has been published recently [55]. Here, only a brief introduction will be given. Figure 1 shows the setup of the new dual GPI system on EAST. It has two imaging objective areas on the low-field side, separated by a toroidal angle of 66.6° and a poloidal angle of roughly 100° around the magnetic axis symmetrically about the midplane. This special arrangement allows the direct measurements of plasma perpendicular flows at two well-separated locations on the same magnetic surface, therefore providing a new diagnostic for ZFs at the plasma edge [57–59]. By definition, the ZFs are uniform flow patterns on the magnetic surfaces with finite radial structures [31, 32].

Helium (He) neutral gas was puffed into deuterium plasmas by a gas manifold for each viewing area through 16 holes of 0.5 mm diameter, spaced by 10 mm perpendicular to the local magnetic field. The visible He I line emission at 587.6 nm from the GPI gas cloud was viewed by two telescopes along the local magnetic field lines to within a few degrees to resolve the radial versus poloidal structure of the turbulence in a 13 cm by 13 cm square area, as shown in figure 1. The blue curve shows the location of the separatrix from the EFIT equilibrium code, which passes through roughly the centre of the two viewing areas. The images were recorded simultaneously by two fast cameras at a frame rate of 390 804 frames s^{-1} and a resolution of 64 × 64 pixels with 12-bit dynamic range for a capturing time of over 250 ms. The brightness of the He I line during the gas puff is more than ten times as high as the background level before the puff, thus localizing the emission for improved spatial resolution. The spatial resolution of the optical system is ∼2 mm at the gas-cloud objective plane, which is smaller than the typical edge-turbulence structure size of 10–30 mm measured by reciprocating probes in EAST [63]. The temporal resolution is 2.56 μs and the exposure time is 2.156 μs per frame, which are much shorter than the typical autocorrelation time of the edge turbulence of 10–20 μs [63]. This time resolution is sufficiently high to capture most of the fluctuation spectrum power.

In the collisional–radiative approximation by ignoring recombination the intensity of the line emission will depend

on the local electron density n_e and temperature T_e as S (photons m^{-3}) $= n_0 f(n_e, T_e) A$ [62], where n_0 is the local neutral density, A is the radiative decay rate for the observed line, and $f(n_e, T_e)$ is a function that gives the density ratio of neutrals in the upper state to the ground state. The decay rate A, being much larger than the inverse of the autocorrelation time of the fluctuations, ensures that the emission corresponds to the local plasma parameters. The functional dependence near the spatial peak of He I light emission in EAST for typical edge parameters, $T_e \sim 30$ eV, $n_e \sim 5\times10^{18}$ m^{-3}, in this experiment, is $S \propto n_e^{\alpha} T_e^{\beta}$, where typically α, $\beta = 0.5$–1 [17, 64, 65]. Although the exponents vary with n_e and T_e in a complex way, the local emissivity S is roughly an indicator of the local electron pressure, p_e. Atomic physics calculations indicated that the response time of these lines to changes in n_e or T_e should be $\leqslant 1\,\mu$s [17].

For this study, the GPI emission data are used to obtain the time-resolved poloidal and radial flow velocities, estimated using a time-resolved 2D cross-correlation analysis code based on a modified time-delay estimation (TDE) technique analogous to the one used previously to evaluate poloidal flows from GPI data in NSTX [12, 15, 66] and C-mod [17, 67]. This technique is also similar to the TDE method previously used to evaluate ZFs from beam emission spectroscopy (BES) turbulence data in DIII-D [68, 69]. Although the GPI light emission is a nonlinear function of the local density and temperature, assuming that the neutral density from the gas puff does not vary on the time scale of the turbulence, the turbulence structures and their motion velocities, as determined by the space–time cross-correlation functions of the GPI light fluctuations, are nearly independent of the details of this nonlinearity, as discussed previously [70]. For each GPI viewing area, the local velocities for each pixel are averaged over the poloidal range of view to evaluate the poloidally averaged large-scale flow component of these velocities.

3. Experimental results from GPI measurements

The L–I–H transitions were captured in three shots (41362, 41363 and 41364) by the newly developed GPI system in the 2012 experimental campaign. The parameters for the three adjacent shots are representative of the usual EAST operating conditions in that campaign. The phenomena in the three shots are generally similar, so here only one shot—No 41363—is presented. It is a double-null discharge with major radius $R_0 = 1.88$ m, minor radius $a = 0.45$ m, elongation factor $\kappa = 1.7$, triangularity $\delta = 0.47$, central-line-averaged density $\bar{n}_e \sim 2.8\times10^{19}$ m^{-3} just prior to the L–I–H transition, toroidal magnetic field $B_t = 1.78$ T on the magnetic axis and plasma current $I_p = 0.4$ MA. B_t and I_p are both in the counter clockwise direction viewing from the top. Figure 1(*a*) shows the plasma configuration at 3.5 s, along with the two GPI viewing areas and the two midplane reciprocating probes [71]. L–I–H transitions are frequently seen in such plasmas with source power of lower hybrid wave current drive (LHCD) $P_{LHCD} = 1.2$ MW at 2.45 GHz, ion cyclotron resonance frequency (ICRF) heating $P_{ICRF} = 1$ MW at 27 MHz, and additional 0.1 MW from ohmic heating. The total effective heating power is ~1 MW, which is slightly above the transition power threshold under such conditions. The ICRF and LHCD

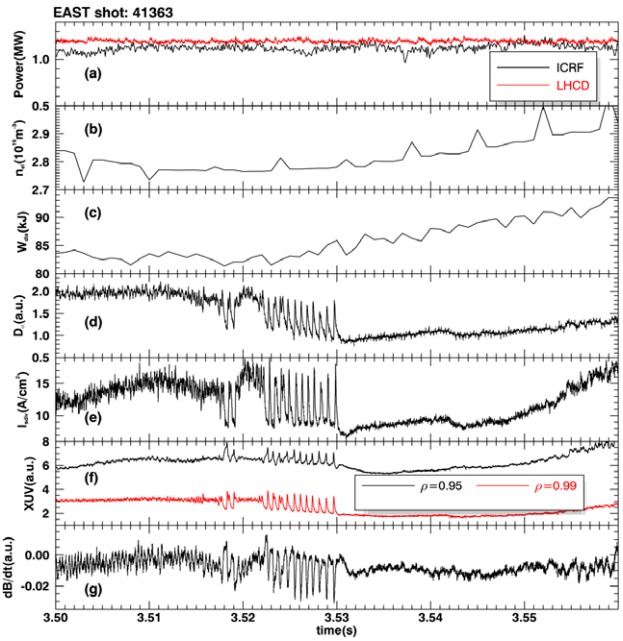

Figure 2. Time history of (*a*) ICRF and LHCD input power, (*b*) central-line-averaged density measured by an HCN laser interferometer, (*c*) diamagnetic stored energy, (*d*) D_α emission from the lower divertor measured by a filter scope, (*e*) ion saturation current measured by a target Langmuir probe near the lower outer strike point, (*f*) XUV signals from the chords passing through $\rho = 0.95$ and 0.99, corresponding to the pedestal top and foot, respectively, (*g*) Mirnov magnetic signal measured at the high-field side midplane.

input powers remain constant during the L–I–H transition, as shown in figure 2(*a*).

The I-phase is characterized by a series of dithering cycles in the D_α emission signals. In shot 41363, a short L–I–L transition with two dithering cycles occurred at 3.518 s, followed by an L–I–H transition with an I-phase from ~3.522 to ~3.530 s, as shown in figures 2(*d*) and 4(*a*) with the divertor D_α signal measured by a filter scope system focusing on the deuterium α line emission at 656.3 nm, installed on top of EAST, viewing the lower divertor region (near X-point) through an upper port. Its sightline is shown in figure 1(*a*). The signal bandwidth for the filter scope system is 0–100 kHz, using photomultiplier tubes (PMTs) as detectors. The behaviour of dithering cycles in the D_α signal during the L–I–L transition is similar to that during the L–I–H transition. For each dithering cycle, it starts with a peak in the D_α signal, passing through an exponential decay phase typically of ~500 μs, then followed by a fast growth phase, which is usually within 100 μs. The decay is on the time scale of the scrape-off layer (SOL) particle confinement, $\tau_\parallel = L_\parallel/(M_\parallel C_s) \sim 500\,\mu$s, where $L_\parallel$ (~10 m) is the SOL parallel connection length, $M_{||}$ (~0.4 measured by a Mach probe mounted on the reciprocating probe system [71]) is the SOL parallel Mach number and $C_s = (2T_e/m_i)^{1/2}$ (~50 km s^{-1}) is the sound speed. The growth phase is much shorter than the decay phase, suggesting that each dithering cycle is terminated with an abrupt enhancement in particle transport at the plasma edge. The reduction in D_α light during the quiescent periods is up to 50% in this shot, indicating a significant improvement in particle confinement at the plasma edge. For L–I–L

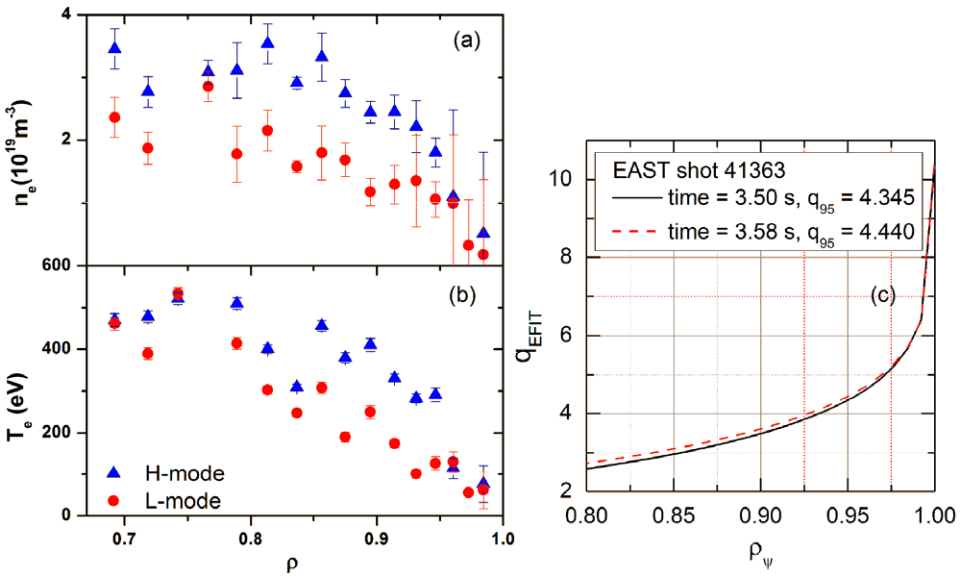

Figure 3. Electron density (*a*) and electron temperature (*b*) profiles measured by the Thomson scattering diagnostic in the L-mode phase (red solid points) and in the H-mode phase (blue solid triangles). (*c*) Safety factor profiles from the EFIT magnetic reconstruction at 3.50 s (before the L–I–H transition) and 3.58 s (after the L–I–H transition).

transitions, the D_α level after the I-phase is usually higher than or the same as that before the I-phase, as seen in figure 2(*a*). However, for L–I–H transitions, the cycle-averaged D_α level in most cases gradually decreases with time, which suggests a progressive enhancement in particle confinement towards the H-mode.

Positive spikes correlated with those in the D_α signal are seen in the ion saturation current measured by a target Langmuir probe near the lower outer strike point, as shown in figure 2(*e*). However, the decay in each dithering cycle of the ion saturation current signals appears to be much faster than that in the D_α signals. The ion saturation current signal is an indicator of the plasma density near the divertor target.

Furthermore, it is interesting to notice in figures 2(*d*) and (*e*) and the enlarged plot near the L–I–H transition in figure 4(*a*) that some small-amplitude oscillations at a frequency of several kHz, considerably higher than the repetition frequency of the normal dithering cycles, appear in the D_α signals and target probe signals preceding the I-phase or between two normal dithering cycles. The observation of such oscillations has been reported recently [13] from EAST, showing that small-amplitude oscillations frequently appear hundreds of milliseconds before L–H transitions or after H–L back transitions when the input heating power is marginal to the transition threshold. The small-amplitude oscillations are usually less regular with respect to the normal large-amplitude dithering cycles during the I-phase, but exhibit similar features of turbulence–flow interactions at the plasma edge.

The central-line-averaged density (figure 2(*b*)) and the diamagnetic stored energy (figure 2(*c*)) start to increase during the I-phase, suggesting that the global particle and energy confinements are improved with respect to the L-mode. Figure 2(*f*) shows the extreme ultra-violet (XUV) radiation signals from the chords passing through $\rho = 0.95$ and 0.99, corresponding to the pedestal top and foot, respectively. In each dithering cycle, the XUV radiation decays at the pedestal foot and grows at the pedestal top, then suddenly collapses, acting like sawteeth. The XUV radiation mostly comes from the bremsstrahlung radiation, which is proportional to $Z_{\rm eff} n_e^2 T_e^{-1/2}$, where $Z_{\rm eff}$ is the effective charge number. Therefore, the behaviour in the XUV signals indicates the periodic build-up and collapse of the density pedestal at the plasma edge.

Figure 2(*g*) shows the Mirnov signal measured at the high-field side midplane. Significant magnetic perturbations (∼1 Gs) correlated with the dithering cycles are detected by the Mirnov coils installed on the chamber wall. These magnetic perturbations are axisymmetric in the toroidal direction, i.e. $n = 0$, confirmed by magnetic measurements from the toroidally distributed Mirnov coils. In the poloidal direction, they have both $m = 0$ and 1 components. Such magnetic perturbations are very likely induced by the periodic accumulation and collapse of the edge pressure gradient during the I-phase due to the magnetohydrodynamic (MHD) equilibrium condition, $\nabla p = \boldsymbol{j} \times \boldsymbol{B}$. The $m = 1$ component could be induced by the perturbations of the Pfirsch–Schlüter current, $j_{\rm PS} = -2r R_0^{-1} B_\theta^{-1} \nabla p \cos\theta$. Note that there are no sawteeth or other MHD activities in this period.

The n_e and T_e radial profiles measured by Thomson scattering diagnostic for the L- and H-mode phases are shown in figures 3(*a*) and (*b*). The n_e and T_e at the top of the pedestal, $\rho = 0.95$, appear to be significantly enhanced across the transition, from ∼1 to $\sim 2 \times 10^{19}$ m^{-3} for n_e and from ∼100 to ∼300 eV for T_e, although T_e in the core region changes little. Figure 3(*c*) shows the safety factor profiles from the magnetic reconstruction with the EFIT code. The safety factor at the flux surface enclosing 95% of the total poloidal flux, q_{95}, increases from 4.345 at 3.50 s (before the L–I–H transition) to 4.440 at 3.58 s (after the L–I–H transition). The slight change in the q profile is mainly due to the broadening of the pressure and current profiles across the transition.

The most important GPI measurement results are shown in figure 4. Figure 4(*b*) shows the time history of the radial

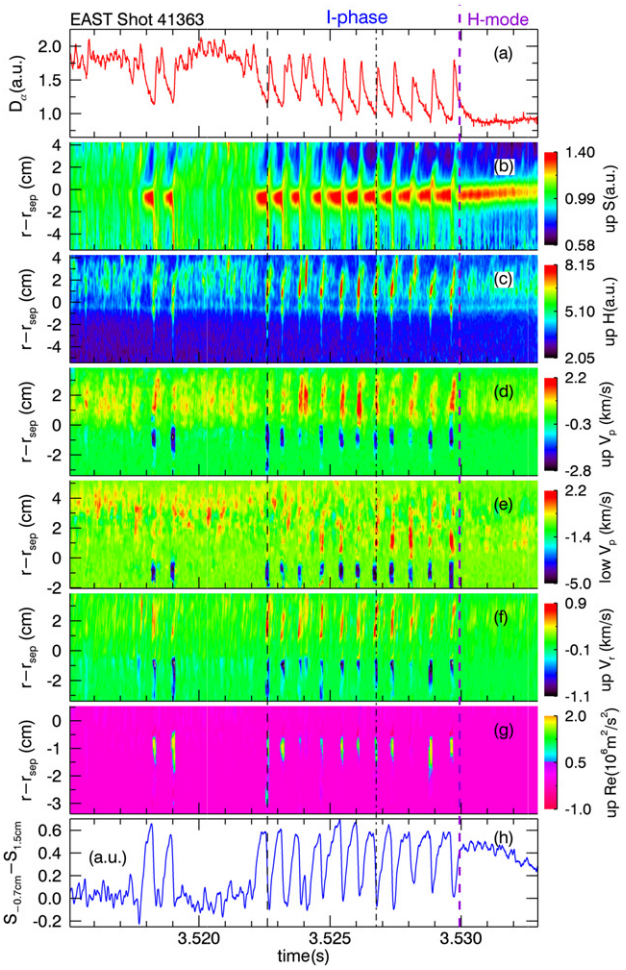

Figure 4. Time evolution of (*a*) divertor D_α emission across a dithering L–H transition, the poloidally averaged radial profiles of (*b*) relative GPI emission intensity, (*c*) turbulence fluctuation level, (*d*) turbulence poloidal velocity from the upper GPI and (*e*) from the lower GPI, (*f*) turbulence radial velocity from the upper GPI, and (*g*) turbulence-driven Reynolds stress from the upper GPI, displayed in a linear false colour scale. (*h*) The difference in the relative GPI emission intensity between two radial locations, i.e. 0.7 cm inside the separatrix and 1.5 cm outside the separatrix.

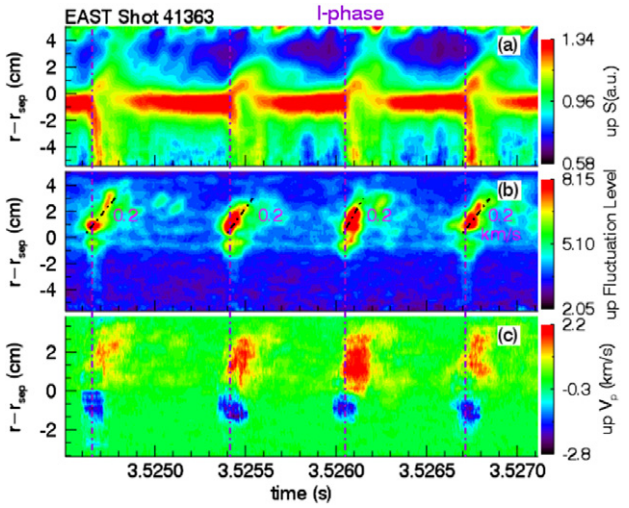

Figure 5. Partially enlarged details of figures 4(*b*), (*c*) and (*d*). The time evolution of the poloidally averaged radial profiles of (*a*) relative GPI emission intensity, (*b*) turbulence fluctuation level, and (*c*) turbulence poloidal velocity from the upper GPI system at the plasma edge during an I-phase, displayed in a linear false colour scale.

profile of relative emission intensity from the upper GPI at the plasma edge, displayed in a linear false colour scale. The intensity images for each frame is normalized by the time-averaged emission intensity over 2 ms during an L-mode period of 3.520–3.522 s, in order to eliminate systematic pixel-to-pixel spatial variations due to neutral distribution and optics. The local relative intensity for each pixel is averaged over the poloidal range of view to remove the poloidal variation. The vertical axis is the distance from the separatrix along the minor radius, i.e. $r - r_{\rm sep}$. Positive sign in the vertical axis corresponds to the region outside the separatrix, i.e. the SOL, with the boundary of the limiter shadow at $r - r_{\rm sep} = 3.6$ cm. Figure 4(*c*) shows the poloidally averaged GPI fluctuation level, which is calculated by applying a high-pass digital filter to remove the fluctuations below 10 kHz, where the dithering cycles dominate the spectrum. There is no perturbation associated with MHD activities, i.e. sawteeth or tearing modes, in the GPI spectrum.

The GPI emission also shows the dithering cycles nearly in-phase with D_α. Further cross-correlation analysis indicates that the dithering cycles in the GPI emission intensity (figure 4(*b*)) and fluctuation level (figure 4(*c*)) lead the divertor D_α by ~100 μs, which is consistent with the SOL parallel heat transport time scale with heat pulses propagating from the GPI locations to the divertor. When a dithering cycle starts the GPI emission intensity appears to decay outside the separatrix on the same time scale of D_α decay, meanwhile grows inside the separatrix, leading to a substantial increase in the intensity gradient near the separatrix. The increase in emission intensity inside the separatrix suggests that the local electron density and/or temperature are enhanced due to the reduced turbulence level and cross-field transport at the plasma edge. The intensity changes appear to originate from the vicinity of the separatrix and expand outwards into the far SOL and inwards into the plasma core, as seen more clearly in the partially enlarged detail in figure 5(*a*), where the tilted patterns indicate the trajectories of propagation.

The difference in the relative GPI emission intensity between two radial locations, i.e. 0.7 cm inside the separatrix and 1.5 cm outside the separatrix, is plotted in figure 4(*h*). The intensity difference grows monotonically during the quiescent period in each dithering cycle, and then suddenly crashes as it reaches a nearly constant threshold level. The flattening of the emission intensity profile is induced by a series of abrupt transient enhancement of turbulence level at the plasma edge (figure 4(*c*)), which terminate the quiescent periods. The duration of the turbulent transient enhancement is usually ~100 μs, which is much shorter than the quiescent period in each dithering cycle.

The fluctuation level appears to be strongly suppressed during the quiescent periods, which blocks the cross-field transport near the separatrix, then opened by the transient enhancement of turbulence. The accumulated plasma pressure inside the separatrix during the quiescent period is rapidly released by the strong turbulent ejection, which finally leads

to a burst in the divertor D_α recycling signals (figure 4(*a*)) via SOL parallel transport. The turbulent transient enhancement appears to originate from the vicinity of the separatrix with clear wave fronts propagating outwards into the far SOL and inwards deeply into the plasma (more than 5.5 cm inside the separatrix, limited by the region reachable by the GPI diagnostic) (figures 4(*b*) and (*c*)), as seen more clearly in the partially enlarged detail in figure 5(*a*). This observation compares favourably with the recent 1D model, showing that the dithering cycle appears to be a nonlinear wave originating from the separatrix and propagating inwards [20, 21].

Space–time patterns of the poloidal motion velocity of turbulence structures from the upper and lower GPI as well as the radial velocity from the upper GPI are calculated using a modified TDE method and are displayed in figures 4(*d*), (*e*) and (*f*), respectively. Positive V_r means the velocity outwards along the minor radius. During the turbulent transient enhancement, the turbulence structures inside the separatrix propagate inwards, while those outside the separatrix propagate outwards at a speed of $\sim 0.2\,\mathrm{km\,s^{-1}}$. The speed is calculated by fitting the slope of the wave-front propagation trajectory, as shown in figure 5(*b*). The error bar for the estimated propagation velocity is $\pm 0.1\,\mathrm{km\,s^{-1}}$. In addition, the GPI emission intensity in the SOL became progressively lower from one dithering cycle to another (figure 2(*b*)), consistent with the gradually reduced D_α level (figure 4(*a*)). This suggests a progressive enhancement in the edge confinement towards the H-mode.

Strong differential poloidal flows appear periodically in a radial range from the SOL up to 2 cm inside the separatrix, accompanying the transient enhancement of turbulence level. The poloidal velocity is accelerated up to $-4\,\mathrm{km\,s^{-1}}$ inside the separatrix and $2\,\mathrm{km\,s^{-1}}$ in the SOL, where negative velocity corresponds to rotation in the direction of electron diamagnetic drift, i.e. downwards at the outer midplane. The generated flows, especially those in the SOL, appear to delay slightly in time with respect to the transient enhancement, as seen in the partially enlarged detail in figure 5, which suggests the causality between them. Correlated poloidal flows observed simultaneously by two GPI cameras at two well-spaced positions on the same magnetic surfaces confirm the ZF characteristics of the flows [31, 32], thus providing strong evidence for ZF generation during the I-phase.

The turbulence Reynolds stress $Re = \langle \tilde{v}_r \tilde{v}_\mathrm{p} \rangle$ [31–33] is directly measured using the GPI during the I-phase, as shown in figure 4(*g*), providing a direct demonstration of nonlinear exchange of energy between turbulence and flows at the plasma edge. Here, the velocity fluctuation levels $|\tilde{v}_\mathrm{p}|$ and $|\tilde{v}_r|$ are $\sim 1\,\mathrm{km\,s^{-1}}$ (half of the peak-to-peak value), estimated from the time-dependent velocities from the upper GPI. Figure 4(*g*) shows that significant Reynolds stress, up to $2\times 10^6\,\mathrm{m^2\,s^{-2}}$, appears during the turbulent transient enhancement in a radial region slightly inside the separatrix, i.e. $r - r_\mathrm{sep} = -2$ to 0 cm.

The Reynolds work performed by the turbulence Reynolds stress on the flows, also known as the energy transfer from turbulence to flows, can be estimated as $W_\perp = \langle \tilde{v}_r \tilde{v}_\mathrm{p} \rangle \langle v_\mathrm{p} \rangle / L_r$ [18, 72, 73], where $L_r \sim 1$ cm denotes the radial gradient scale length, estimated from the GPI measured $\langle v_\mathrm{p} \rangle$ profiles near the separatrix. The poloidal velocity shear near the separatrix is measured to be $\langle v_\mathrm{p} \rangle / L_r \sim 5 \times 10^5\,\mathrm{s^{-1}}$. Thus, the Reynolds work is estimated to be $W_\perp \sim 1 \times 10^{12}\,\mathrm{m^2\,s^{-3}}$. Reynolds work gives a measure of the amount of kinetic energy per unit mass and unit time that is transferred between turbulence and flows. Positive $W_\perp$ means net energy is transferred from turbulence into flows, so that the flows are amplified at the expense of the turbulence kinetic energy, while negative means energy is transferred from flows back into turbulence resulting in flow damping. Therefore, the generation process of flows directly provides a suppression mechanism of turbulence, leading to a net decay of turbulence energy. The estimated energy transfer rate $W_\perp / |\tilde{v}_r|^2 \sim 1 \times 10^6\,\mathrm{s^{-1}}$ is significantly higher than the typical collisional damping rate of flows ($\sim 2 \times 10^4\,\mathrm{s^{-1}}$) or the turbulence decorrelation rate ($\sim 1 \times 10^5\,\mathrm{s^{-1}}$) at the plasma edge, measured by reciprocating probes in EAST [13, 19, 74].

The equation for the evolution of poloidal flow takes the form $\varepsilon_\perp \partial \langle v_\mathrm{p} \rangle / \partial t = \partial \langle \tilde{v}_r \tilde{v}_\mathrm{p} \rangle / \partial r + \cdots$ [75, 76], where $\cdots$ indicates additional effects, such as a collisional damping term. Here, the coefficient $\varepsilon_\perp$ denotes the relative dielectric constant for E_r, i.e. the ratio between the dielectric constant to that of vacuum ε_0. The collisionality in the plasma edge is in the plateau regime, so that $\varepsilon_\perp$ is given as $1 + 2q_{95}^2 \approx 40$ for $q_{95} = 4.4$ [75, 76]. The time scale for the poloidal flow acceleration is $\tau \sim 200\,\mu\mathrm{s}$ during the one dithering cycle. From the equation, by using the above parameters, the poloidal flow driven by the radial gradient of the Reynolds stress is evaluated as $\delta \langle v_\mathrm{p} \rangle = \tau \langle \tilde{v}_r \tilde{v}_\mathrm{p} \rangle / (L_r \varepsilon_\perp) \sim 1\,\mathrm{km\,s^{-1}}$, which is in reasonable agreement with the oscillatory poloidal velocity measured by the GPI in the I-phase.

Furthermore, the energy gain by the global flows at the plasma edge in one dithering cycle is estimated to be $0.5 m_\mathrm{i} \varepsilon_\perp \langle v_\mathrm{p} \rangle^2 \sim 10\,\mathrm{eV/ion}$ [13, 19, 74], which is of the same order as the turbulence energy loss during the suppression, $e|\tilde{\phi}| + 0.5 m_\mathrm{i} |\tilde{v}_\perp|^2 \sim 10\,\mathrm{eV/ion}$, where $|\tilde{\phi}| \sim 10\,\mathrm{V}$ is the plasma electrostatic potential fluctuation level, and the kinetic energy of the $\boldsymbol{E} \times \boldsymbol{B}$ flow fluctuation, $0.5 m_\mathrm{i} |\tilde{v}_\perp|^2$, is small with respect to $e|\tilde{\phi}|$. Therefore, the energy transfer from turbulence to flows is sufficiently strong to account for the observed flow generation during the I-phase.

Following a turbulent transient enhancement, the turbulence is quickly damped (figures 4(*c*) and 5(*b*)), possibly because its driving force—the pressure gradient—is weakened by the turbulent transient enhancement, which terminates the turbulent state and initiates a quiescent period. The differential poloidal flows decay subsequently (figure 5(*c*)), possibly due to the loss of turbulent drive. To a certain point, the turbulence level recovers, followed by the initiation of the next dithering cycle.

In addition, some small-amplitude oscillations in D_α, preceding the L–I transitions or between two dithering cycles, act like a transition precursor, and appear to correlate with the oscillations in the turbulence fluctuation level (figure 4(*c*)), the relative GPI emission intensity (figure 4(*b*)) and difference (figure 4(*h*)), as well as the turbulence-driven flows (figures 4(*d*), (*e*) and (*f*)). Although with a smaller amplitude, these oscillations exhibit similar features of turbulence–flow interactions at the plasma edge, e.g. the oscillation (small negative spikes in D_α) at 3.5174 s prior to an L–I transition or at 3.5241 s between two dithering cycles. These small-amplitude oscillations, manifested as small-sized dithering cycles, which have long been ignored previously, may be important for understanding the transition dynamics.

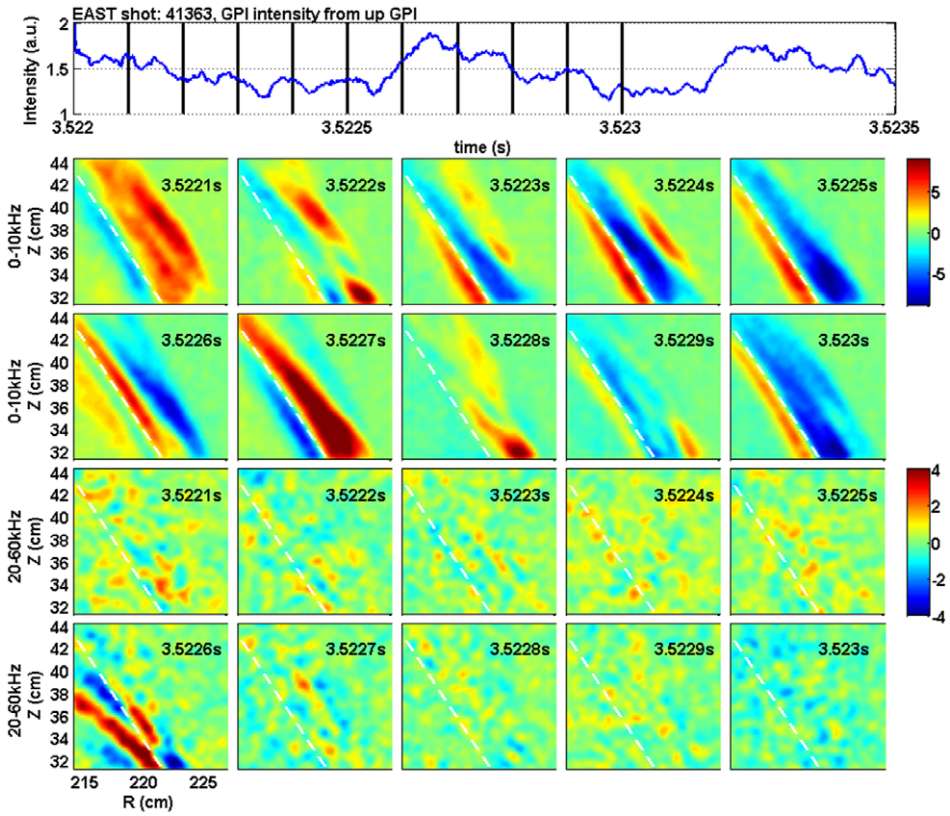

Figure 6. Time sequence of filtered images from the up GPI in one dithering cycle at 10 time slices with 100 μs interval, as marked with the vertical lines in the top plot, where the time history of one-pixel GPI emission intensity in the near SOL is displayed. The images in the first two lines are low-frequency perturbations below 10 kHz, where the mean value for each pixel is removed. The images in the last two lines are high-frequency perturbations in the frequency band 20–60 kHz. The white dashed line shows the separatrix.

Figure 6 shows the time sequence of filtered 2D images from the up GPI in one dithering cycle at 10 time slices with 100 μs interval, as marked with the vertical lines in the top plot, where the time history of one-pixel GPI emission intensity in the near SOL is displayed. The images in the first two lines are low-frequency perturbations below 10 kHz. To enhance the contrast, the mean value for each pixel is removed. The images in the last two lines are high-frequency fluctuations in the frequency band 20–60 kHz. The turbulent fluctuations appear during the turbulent transient enhancement peak at ~40 kHz in the frequency domain; the 20–60 kHz frequency band covers most of the spectral power of the turbulent fluctuations in the GPI signals. The white dashed line shows the separatrix.

From the low-frequency perturbations, one can see the progressive build-up of a gradient of the GPI emission intensity right near the separatrix with increasing intensity inside the separatrix and decreasing intensity outside the separatrix. During this quiescent period, the high-frequency fluctuations exhibit a low fluctuation level and nearly random fluctuation pattern. When the turbulent transient enhancement occurs, as indicated by the images taken at 3.5226 s, a strongly elongated and tilted structure appears just inside the separatrix in the high-frequency image with a significantly enhanced fluctuation level. This structure propagates poloidally in the electron diamagnetic direction, i.e. downwards in the image. At the same time, the gradient near the separatrix collapses, as shown in the low-frequency images. The GPI intensity is significantly reduced inside the separatrix and enhanced outside the separatrix. This intensity exchange is further strengthened at 3.5227 s, when the fluctuation structure in the high-frequency image disappears. It initiates another quiescent period with the GPI intensity gradient building up again near the separatrix.

The above observations generally support the theory that turbulence-driven ZFs play a role in generating the LCOs during the L–H transition [30]. However, the transition cannot be interpreted solely by the ZFs. ZFs may play an important role in mediating the L–H transition but cannot maintain the H-mode state, since the existence of ZFs relies parasitically on the kinetic energy of turbulence. In the absence of a turbulent drive, ZFs will quickly die away. There is another player—the EF shear, which is not driven by turbulence. The EF shear usually builds up as the auxiliary heating power is switched on or ramps up, due to the steepening of the edge pressure gradient. It can suppress the edge turbulence due to the well-known shear decorrelation mechanism [36–38], thus push the plasma system towards the transition boundary. During an L–I–H transition, the transient reduction in turbulence and transport by ZF shear during the quiescent periods will allow the edge pressure gradient and therefore the EF shear to increase slowly, which could finally terminate the I-phase and lock in the H-mode state.

Figures 7(*a*) and (*b*) show the time evolution of turbulence poloidal velocity (V_p) and velocity shearing rate ($\partial V_\mathrm{p}/\partial r$) across the plasma edge in an expanded time window of the same shot as in figure 4. The time windows for the I-phases

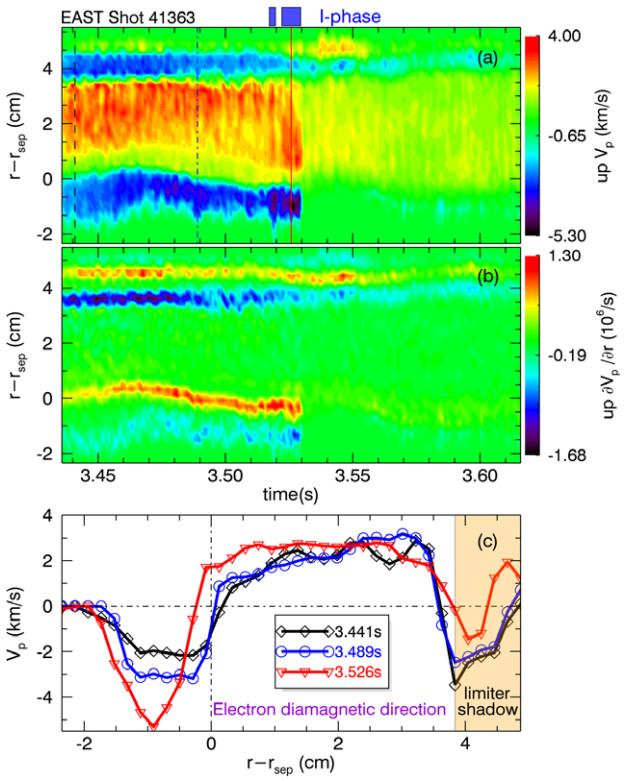

Figure 7. Time evolution of the poloidally averaged radial profiles of (*a*) turbulence poloidal velocity, V_p, and (*b*) shearing rate of the poloidal velocity, $\partial V_\mathrm{p}/\partial r$, from the upper GPI system at the plasma edge across a dithering L–H transition, displayed in a linear false colour scale. (*c*) Radial profiles of poloidal velocity, corresponding to the time slices marked as vertical lines in (*a*). The blue colour bars at the top indicate the time windows for the I-phases shown in figure 2.

in figure 4 are marked as blue colour bars at the top of figure 7(*a*). The auxiliary heating power was switched on at 3.240 s, nearly 290 ms before the H-mode transition (at 3.530 s). During this period, the plasma density was slowly rising from $\bar{n}_\mathrm{e} \sim 2.0$ to $\sim 2.8 \times 10^{19}\,\mathrm{m}^{-3}$ just prior to the H-mode transition (figure 2(*b*)), and the plasma stored energy increased from $W_\mathrm{dia} \sim 65$ to 83 kJ (figure 2(*c*)). As seen in figure 7, the poloidal velocity and its shear on both sides of the separatrix slowly increase on a time scale of tens of milliseconds on approaching the final H-mode transition. This slowly evolving poloidal flow may be associated with the EF, i.e. the equilibrium flow. It is impossible to separate the turbulence-driven flow and the EF from the total GPI measured poloidal flow. However, the GPI fluctuation level does not show significant increase on approaching the transition, which may imply that the turbulence driving force does not increase significantly prior to the transition. Therefore, the mean growing contribution from the turbulence-driven flow could be small with respect to the EF increment. The role of the increasing background equilibrium driven velocity shear in triggering the L–H transition has been experimentally demonstrated recently on ASDEX-Upgrade [40, 41] and previously on DIII-D [77]. This slow increase in the poloidal velocity and its shear has been seen in the three shots currently available with GPI measurements. For each time slice in figure 7, the velocity is calculated with 800 frames, i.e. time-averaged over ∼2 ms, to obtain the velocity profile in the poloidal–radial plane versus time, then averaged over the poloidal range of view to remove the poloidal variation. However, in H-mode, the turbulence fluctuation level is significantly suppressed so that there is insufficient statistics for the velocity analysis based on the TDE method. As a result, the poloidal velocity and its shear appear to be unreasonably small in the H-mode phase.

Figure 7(*c*) shows the radial profiles of poloidal velocity, corresponding to three typical time slices marked by vertical lines in figure 7(*a*). The velocity is in the electron diamagnetic direction inside the separatrix and in the ion diamagnetic direction in the SOL, consistent with the observations in many other tokamak experiments [78]. The ion diamagnetic direction velocities in the SOL are normally due to the sheath potential being positive and falling with radius as T_e decreases. In figure 7(*c*), the poloidal velocity initially exhibits a U-shaped structure of 2 cm in width right inside the separatrix. The bottom of the U-shaped structure evolves slowly with time from $-2\,\mathrm{km\,s}^{-1}$ in L-mode to $-5\,\mathrm{km\,s}^{-1}$ in the I-phase just prior to the H-mode transition. In the limiter shadow area, the calculated velocity is in the electron diamagnetic direction, and the reason for this is unclear.

No GAM near its characteristic frequency $f_\mathrm{GAM} = \alpha_\mathrm{GAM} C_\mathrm{s}/R \sim 20$ kHz is found in either GPI or reciprocating Langmuir probe data near the L–H transitions, where α_GAM is a numerical factor depending on the plasma shape. The GAM, frequently observed in L-mode and ohmic plasmas in EAST, usually disappears as the L–H transition threshold conditions are approached. Similar observations were reported previously from DIII-D with BES measurements [27, 28] and HL-2A with probes [29]. In addition, no precursor MHD coherent modes prior to each dithering cycle like those frequently appearing prior to type-III edge-localized modes (ELMs) are observed in either GPI or reciprocating Langmuir probe signals. This could be an important distinction between the dithering cycles and type-III ELMs.

4. Modelling of the L–I–H transition

The aforementioned GPI data show sawtooth-like behaviour near the separatrix during the I-phase, i.e. gradual build-up and sudden exchange of pressure between the inner side and outer side of the separatrix. The GPI observations strongly suggest that the SOL transport physics and the evolution of pressure gradient near the separatrix may play an important role in the L–I–H transition dynamics. The pressure gradient near the separatrix is proportional to the pressure difference between the inner side of the separatrix and the SOL. It is found in the experiments that the build-up of pressure gradient near the separatrix is contributed both by the increment of pressure inside the separatrix and the reduction of pressure in the SOL. When the turbulent transient enhancement occurs, the pressure gradient near the separatrix collapses. Particles and heat are exhausted across the separatrix, flattening the local pressure gradient, making the SOL pressure increase and the pressure inside the separatrix decrease. The time evolution of SOL pressure is controlled by the SOL parallel transport physics. To highlight these new physics, the previous 0D predator–prey model [30] is extended to include a new equation for the SOL

physics. The contribution of the SOL pressure evolution to the EF has been included, for the first time, in this model. The model incorporates the time evolution of plasma pressure on both sides of the separatrix, turbulence intensity, EF shear, ZF shear, and successfully reproduces the L–I–H transition process with several features comparing favourably with the GPI observations. Here, the turbulence intensity refers to the root mean square (RMS) level of density fluctuations. This model consists of four coupled equations:

$$\partial_t p_{\rm edge} = Q - q - q_{\rm neo} \tag{1}$$

$$\partial_t p_{\rm sep} = q + q_{\rm neo} - p_{\rm sep}/\tau_{\parallel} \tag{2}$$

$$\partial_t I = \gamma q I - \alpha V^2 I \tag{3}$$

$$\partial_t V = \beta I V - \mu (V - U). \tag{4}$$

Here, equations (1) and (2) describe the time evolution of the pressure inside the separatrix, $p_{\rm edge}$, and at the separatrix, $p_{\rm sep}$, respectively. The pressure at the plasma edge, $p_{\rm edge}$, is enhanced by the power influx from the plasma core, Q, but reduced by the power outflux through turbulent transport, q, and neoclassical transport, $q_{\rm neo}$, with q much larger than $q_{\rm neo}$ in L-mode but strongly suppressed in H-mode. One new feature distinguishing the model from the previous predator–prey model of the L–H transition [30] is that the SOL physics has been included in equation (2). It plays an important role in the transition dynamics, as will be shown later in this paper. In the SOL, the imbalance between the power influx through the cross-field transport across the separatrix, $q + q_{\rm neo}$, and the power outflux through parallel transport on a time scale of the parallel communication time from the low-field side midplane to the divertor target plate, $\tau_{\parallel}$, drives the time evolution of $p_{\rm sep}$. The SOL parallel transport time scale $\tau_{\parallel}$ is found to control the cycle duration when $\tau_{\parallel}$ is shorter than the $p_{\rm edge}$ relaxation time scale, which shows the importance of the SOL parallel transport to the LCO dynamics. Both the turbulent flux and the neoclassical flux are assumed to be driven by the pressure gradient near the separatrix, i.e. $q = \chi I \Delta p$ and $q_{\rm neo} = \chi_{\rm neo} \Delta p$, where $\Delta p = p_{\rm edge} - p_{\rm sep}$ is the pressure difference at the plasma edge, I is the turbulence intensity and χ is the thermal transport coefficient.

The time evolution of the turbulence intensity, I, and the flow shear near the separatrix, $V \propto \partial_r V_{E\times B}$, are controlled by equations (3) and (4), respectively, by extending the previous 0D predator–prey LCO model [30] to combine the contributions from EF shear and ZF shear in one term, i.e. $\alpha V^2 I$, which represents the Reynolds energy transfer from the turbulence to the flows. The total flow shear, V, is composed of the EF shear, $U \propto \partial_r V_{\rm EF}$, and the ZF shear, $V - U \propto \partial_r V_{\rm ZF}$, where $V_{\rm EF} + V_{\rm ZF} = V_{E\times B}$. Here, all turbulence-driven flows are classified as ZFs. The above set of equations is closed by the following expression of EF shear, $U = \kappa \Delta p$. The EF arises from the equilibrium, and is, to leading order, balanced by the ion diamagnetic term in the radial force balance equation, therefore proportional to the pressure gradient. The physics of inhibiting the ZF shear by the EF, which appears in the previous model [30], is not included in this model. This physics is unnecessary for the occurrence of the L–I–H transition, as demonstrated by the new model.

The free energy stored in the pressure gradient is released and part of this is deposited in the turbulence through equation (3). The turbulence in this model is assumed to be flux driven and suppressed by the flow shear due to transfer of kinetic energy from the turbulence into the sheared flows via the Reynolds work, so that the first term on the right-hand side of equation (3) is proportional to q and the second term is proportional to V^2. The transferred energy then drives the sheared flows through the first term on the right-hand side of equation (4), following the expression in [30]. Finally, the energy is released through dissipation, as described by the last term in equation (4), where the sheared flows are subjected to strong frictional damping. Here, μ is the total flow damping rate, including damping effects from collision, charge exchange, neutral friction and other nonlinear mechanisms. According to equation (4), in the absence of turbulence ($I \to 0$), such as in the case of H-mode, the flow shear, V, will relax towards the EF shear, U, since in the absence of turbulent drive, the ZF shear, $(V - U)$, is going to vanish.

This system of equations is solved numerically based on an explicit four-order Runge–Kutta method, starting from an L-mode non-oscillatory state, evolving across an I-phase and ending with a quiescent H-mode. Figure 8 shows the modelling results, including the time evolution of pressure at the separatrix ($p_{\rm sep}$) and inside the separatrix ($p_{\rm edge}$), edge

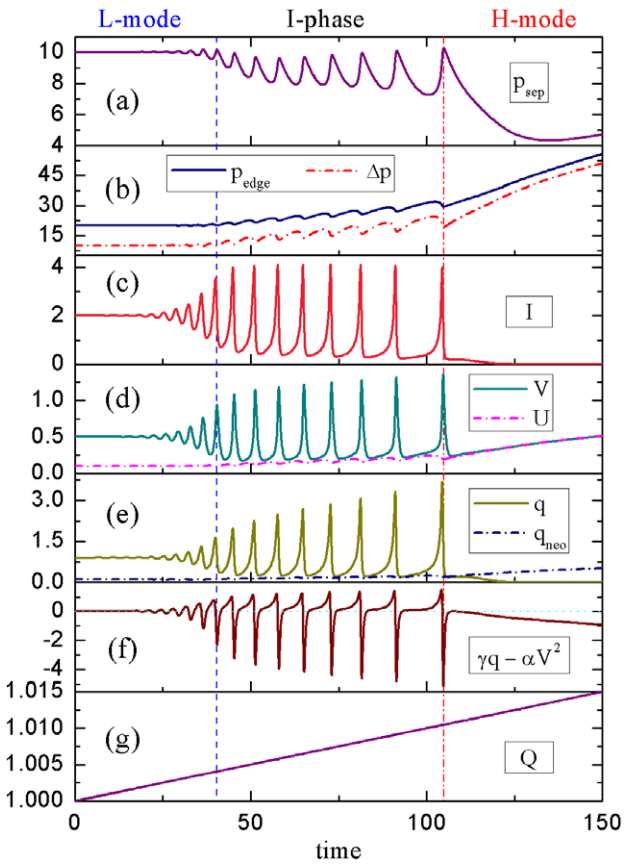

Figure 8. Modelling of the L–I–H transition with a self-consistent 0D model. The time evolution of (*a*) pressure at the separatrix, $p_{\rm sep}$, (*b*) pressure inside the separatrix, $p_{\rm edge}$, and edge pressure difference, $\Delta p = p_{\rm edge} - p_{\rm sep}$, (*c*) turbulence intensity, I, (*d*) total flow shear, V, and EF shear, U, (*e*) turbulent flux, q, and neoclassical flux, $q_{\rm neo}$, (*f*) imbalance between the drive and damping of turbulence, (*g*) input heating power flux, Q.

pressure difference (Δp), turbulence intensity (I), total flow shear (V), EF shear (U), turbulent flux (q), neoclassical flux ($q_{\rm neo}$), imbalance between the drive and damping of turbulence on the right-hand side of equation (3), and input heating power flux (Q), assuming constant values for the other coefficients. The external control parameter of the system is Q, which is the source of free energy. It increases from unity at a slow ramping rate of $10^{-4}\times$time, as shown in figure 8(g).

This system of equations has two stationary solutions with Q fixed at two constant values, corresponding to two non-oscillatory states. One is the H-mode, for which the turbulence intensity and the turbulent flux vanish. Without the turbulent transport, the input heating power can only be carried out through the neoclassical flux, $q_{\rm neo} = Q$, so that the edge pressure gradient is determined solely by the neoclassical transport, $\Delta p = Q/\chi_{\rm neo}$. In the SOL the neoclassical flux is balanced by the parallel flux, which makes the SOL pressure dependent on Q, i.e. $p_{\rm sep} = \tau_{||} Q$. The pressure inside the separatrix is therefore proportional to Q with $p_{\rm edge} = Q/\chi_{\rm neo} + \tau_{\|} Q$. In addition, the flow shear is clamped to the EF shear, i.e. $V = U$, which is also an increasing function of Q.

The other non-oscillatory state is the L-mode, which is characterized by a finite level of turbulence and turbulent flux. A set of initial values, which satisfies the set of equations for an L-mode non-oscillatory state, is applied to the L–I–H transition model, as listed in table 1. The third column of table 1 shows the corresponding actual experimental parameters of the EAST plasmas. The space unit for the normalization in the model is $\delta r = 2\,$cm, which is the radial gradient scale length near the separatrix. The time unit for the normalization is $\delta t = R_0/C_{\rm s} = 40\,\mu$s, where the EAST major radius is $R_0 \sim 2\,$m and the ion sound speed near the separatrix is $C_{\rm s} \sim 50\,{\rm km\,s^{-1}}$. With this time unit, the duration for the I-phase is ~3 ms and the average period for one dithering cycle is ~0.5 ms, as shown in figure 8. The loss power across the plasma boundary is about 1 MW in the aforementioned EAST experiments. The plasma surface area is $40\,{\rm m^2}$. Therefore, the power flux across the plasma boundary is $1\,{\rm MW/40\,m^2}$, in which $0.1\,{\rm MW/40\,m^2}$ is through the neoclassical transport channel and $0.9\,{\rm MW/40\,m^2}$ is through the turbulent transport channel. The plasma pressure at the separatrix and inside the separatrix are $p_{\rm sep} = 500\,{\rm J\,m^{-3}}$ and $1000\,{\rm J\,m^{-3}}$, respectively. The pressure gradient near the separatrix is $\Delta p = 2.5\times10^4\,{\rm J\,m^{-4}}$. The neoclassical and turbulent transport coefficients at the plasma edge are $\chi_{\rm neo} = 0.1\,{\rm m^2\,s^{-1}}$ and $\chi I = 0.9\,{\rm m^2\,s^{-1}}$, respectively. The total $\boldsymbol{E}\times\boldsymbol{B}$ flow shear and the EF shear are $2.5\times10^5\,{\rm s^{-1}}$ and $5\times10^4\,{\rm s^{-1}}$, respectively, corresponding to an EF at $1\,{\rm km\,s^{-1}}$ in the L-mode.

The evolution of the system starts from an L-mode stationary equilibrium state defined by the above set of initial values. If the input heating power, Q, is fixed at 1, the system will stay in the initial L-mode state forever. All parameters and variables will remain constant. The initial L-mode state is stable and robust against small variations of the initial values. As Q slowly ramps up linearly, the system passes through three distinct phases, as indicated in figure 8. The early phase is an L-mode, during which small-amplitude oscillation appears and grows into normal dithering cycles after several oscillation periods. Such small-amplitude oscillations prior to I-phase or L–H transition have been observed in experiments, as shown in figure 4(a), described in section 3.

Table 1. A set of initial values for the L-mode stationary solution of the L–I–H transition model.

Variable	Initial value in the model	Corresponding experimental parameters
δr space unit	1	2 cm
δt time unit	1	40 μs
$\tau_{\|}$	10	400 μs
Q	1	$1\,{\rm MW/40\,m^2}$
Q	0.9	$0.9\,{\rm MW/40\,m^2}$
$q_{\rm neo}$	0.1	$0.1\,{\rm MW/40\,m^2}$
$p_{\rm sep}$	10	$500\,{\rm J\,m^{-3}}$
$p_{\rm edge}$	20	$1000\,{\rm J\,m^{-3}}$
Δp	10	$2.5\times10^4\,{\rm J\,m^{-4}}$
$\chi_{\rm neo}$	0.01	$0.1\,{\rm m^2\,s^{-1}}$
χ	0.045	$0.45\,{\rm m^2\,s^{-1}}$
I	2	2
V	0.5	$2.5\times10^5\,{\rm s^{-1}}$
U	0.1	$5\times10^4\,{\rm s^{-1}}$
κ	0.01	$2\,{\rm m^4\,s^{-1}\,J^{-1}}$
μ	2.5	$62\,500\,{\rm s^{-1}}$
β	1	$25\,000\,{\rm s^{-1}}$
γ	1	$1\,{\rm m^2\,J^{-1}}$
α	3.6	$3.6\times10^{-7}\,{\rm s}$

The L-mode phase is followed by an I-phase, characterized by dithering cycles. The time waveform of $p_{\rm sep}$ (figure 8(a)) resembles the D_α waveforms very much, since the pressure drives the SOL parallel flows and therefore the divertor D_α emission from the recycling neutrals. It is interesting to notice in figure 8 that the cycle period increases with time on approaching the final H-mode transition. This phenomenon is frequently seen in our experiments, which could be due to progressive enhancement of the EF shear during the I-phase.

The I-phase is finally terminated by a transition into the H-mode phase, with significantly suppressed turbulence and turbulent flux (figures 8(c) and (e)), leading to a fast growth of the pressure inside the separatrix and the edge pressure gradient (figure 8(b)). The neoclassical transport then takes over from the turbulent transport with the flow shear, V, tracking the EF shear, U, closely (figure 8(d)). The final transition from I-phase to H-mode occurs when a threshold level in the EF shear, U, is crossed, followed by a progressive enhancement in the edge pressure gradient, Δp, during the I-phase. Finally, if the input heating power, Q, stops increasing and is fixed at a constant value (higher than the L-mode value) an H-mode stationary equilibrium state will be reached eventually.

By comparing with the experimental results shown in figure 4, one can see that the time evolutions of the pressure $p_{\rm edge}$ and $p_{\rm sep}$, pressure gradient Δp, turbulence intensity I and flow shear V from the modelling are in good agreement with the GPI experimental observations, as shown in figure 4(b) GPI emission intensity, (h) intensity gradient, (c) fluctuation level, (d) and (e) poloidal velocities. The model successfully reproduces the sawtooth-like behaviour with pressure exchange between the inner side and outer side of the separatrix during the I-phase, which is new to this paper and consistent with the most important new finding from the GPI measurements. According to equation (2), the decay of $p_{\rm sep}$ and therefore the D_α emission across the H-mode transition or during the decay phase of each dithering cycle is on the time scale of the SOL parallel loss, $\tau_{\|}$, consistent with experiments.

Furthermore, the time scale for the growth phase of p_{sep} during one dithering cycle, i.e. that for replenishing the SOL by the turbulent transient enhancement, is much shorter than the decay phase, and the cycle-averaged p_{sep} appears to decrease progressively during the I-phase as the final H-mode transition is approached, again comparing favourably with experiments, as shown in figure 4(a), described in section 3. In addition, the slow rising of the pressure inside the separatrix and the edge pressure gradient during the I-phase (figure 8(b)), together with the gradual reduction in the cycle-averaged p_{sep}, suggest a progressive enhancement in the edge confinement towards the H-mode.

With the help of the model, we are allowed to have a deeper insight into the physics behind the L–H transition. The ZFs have been proposed as a candidate for triggering the transition in the popular theory [30]. The energy transfer from turbulence to ZFs can lead to the suppression of turbulence level as well as ZF generation. In the L-mode non-oscillatory state, it has been shown in experiments that finite energy transfer from turbulence to ZFs exists at the plasma edge, which maintains a saturated level of low-frequency ZFs [29, 32, 57–59, 71]. At the transition to the H-mode or in the quiescent period of a dithering cycle, a mechanism is required to initiate a fast energy transfer process or other turbulence damping processes, so that the edge turbulence can be quenched in a short period. However, since the ZF is turbulence driven, it cannot suppress the turbulence alone without a pronounced overshoot in the ZF amplitude or a sharp increase in the energy transfer rate from turbulence to ZFs. If there is an overshoot in the ZF amplitude, a transient enhancement of turbulence is required prior to the overshoot to drive the ZFs so that they have sufficient amplitude to quench the turbulence. The puzzle is not regarding the causality between turbulence suppression and ZF generation, since they occur simultaneously during the energy transfer process, but regarding what initiates the fast energy transfer process across the transition.

This puzzle can be solved when another player is taken into account, i.e. the EF shear. The successful reproduction of an L–I–H transition by the above modelling suggests that the transition and the oscillatory behaviour during an I-phase could be induced by the synergistic effect of the ZF and the EF, instead of solely by the action of ZF. As indicated by the model, two feedback loops exist at the plasma edge, associated with the two flow components, i.e. the ZF and the EF, respectively, through which the fast energy transfer process and turbulence suppression at the transition are initiated.

Figure 9 shows a schematic block diagram of the two feedback loops in the model. The oscillatory behaviour and fast energy transfer at the transition are controlled by a fast feedback loop associated with the ZF shear, $(V - U)$, which cannot be activated by itself when the system is far below the transition threshold. It needs another feedback loop, i.e. that associated with the EF shear, to push the system towards the transition boundary. The latter is a positive feedback loop, evolving on the time scale of local transport, which is much slower compared with the dithering cycle period.

As the transition threshold is approached, heat and particles accumulate at the plasma edge with increasing heating power, Q, resulting in an increase in the pressure inside the separatrix, $\langle p_{edge}\rangle$, which drives the EF shear, $\langle U\rangle$, where

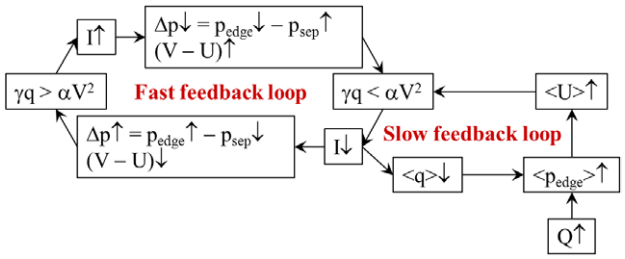

Figure 9. Schematic block diagram of the two feedback loops in the 0D L–I–H transition model. The fast and slow feedback loop is associated with the ZF shear, $(V - U)$, and the EF shear, $\langle U\rangle$, respectively, where $\langle\cdots\rangle$ denotes the time average over a dithering cycle period.

$\langle\cdots\rangle$ denotes the time average over a dithering cycle period. The EF shear promotes the energy transfer from turbulence to ZFs through the Reynolds work. When the energy loss of the turbulence exceeds the energy gain, i.e. $\gamma q < \alpha V^2$, the turbulence starts to be suppressed, which initiates the dithering cycles in the fast feedback loop. On the other hand, the cycle-averaged turbulent flux, $\langle q\rangle$, is reduced, which then further enhances the pressure inside the separatrix, $\langle p_{edge}\rangle$, enabling the system to evolve towards the H-mode. This positive feedback loop controls the transition direction. This evolution direction can be reversed if the power flux, Q, ramps down instead of ramping up. Any perturbation in Q, such as the transient enhancement in power flux by a sawtooth heat pulse [79], can accelerate or slow down the positive feedback, and therefore promote or delay the transition process.

For the fast feedback loop, dithering cycles are activated only when the transition power threshold is approached. The oscillation can be amplified, as seen in figure 9, since free energy stored in the pressure gradient can be fed into the turbulence–ZF system through the turbulence drive. In our experiments, dithering cycles with increasing oscillation amplitudes towards the final H-mode transition are frequently observed.

A dithering cycle starts with turbulence suppression, $I\downarrow$, which initiates a quiescent period. Heat and particles are accumulated inside the separatrix, enhancing the edge pressure, $p_{edge}\uparrow$, as the cross-field transport at the plasma edge is suppressed. In the SOL, since the particle and heat source are reduced, the pressure decays, $p_{sep}\downarrow$, on the time scale of the SOL parallel loss, $\tau_{\|}$, together with the enhanced p_{edge}, leading to an increase in the pressure gradient near the separatrix, $\Delta p\uparrow$, which then enhances the turbulence drive. On the other hand, with reduced ZF drive, the flow shear, V, relaxes towards the EF shear, U, i.e. the ZF shear is damped subsequently, $(V - U)\downarrow$, which then reduces the damping of turbulence. To a certain point, the combined effects make the turbulence drive exceed the turbulence damping, i.e. $\gamma q > \alpha V^2$ (figure 8(f)), so that the turbulence starts to grow in intensity, i.e. $I\uparrow$. This growth eventually evolves into a transient enhancement of turbulence, as shown in figure 8(c).

The cross-field transport, which is blocked during the quiescent period, is then opened by the transient enhancement of turbulence (figure 8(e)). The accumulated pressure inside the separatrix, p_{edge}, during the quiescent period is rapidly released by the strong turbulent ejection, which flattens

the pressure profile near the separatrix (figure 8(*b*)), and replenishes the SOL with fresh particles and heat, leading to a quick recovery of the pressure at the separatrix, p_{sep} (figure 8(*a*)). At the same time, pronounced ZF shear, $(V - U) \uparrow$, is driven by the turbulent transient enhancement (figure 8(*d*)), which significantly enhances the damping of turbulence. Meanwhile, the turbulence drive is weakened due to the reduced pressure gradient, $\Delta p \downarrow$, so that the turbulence damping exceeds the turbulence drive very quickly, i.e. $\gamma q < \alpha V^2$ (figure 8(*f*)), leading to a sharp decay in the turbulence intensity (figure 8(*c*)) and the turbulent flux (figure 8(*e*)). During this process, the free energy stored in turbulence is transferred into the ZFs via the Reynolds work, driving the ZF shear, and finally released through ZF damping. When the turbulence is suppressed, i.e. $I \downarrow$, the system evolves into a quiescent period again. Then, a new dithering cycle starts. Finally, the I-phase is terminated by a sharp transition into the H-mode, as the EF shear, U, is sufficiently strong to take over from the ZF shear, stopping the recovery of the turbulence intensity, and thus locking in the H-mode state. The important role of the EF shear in determining the final transition point has been experimentally demonstrated recently on ASDEX-Upgrade [40, 41] and previously on DIII-D [77].

The sensitivity of model results to the fixed coefficients is studied. For instance, it is found that the coefficient β controls the number of repetitive cycles in the I-phase. With increasing β, the number of repetitive cycles increases, since the ZF drive is strengthened, which delays the EF take-over time. The coefficient α cannot change independently, since it must change with the turbulence growth rate γ to satisfy the equation for an L-mode stationary state. More discussions on the sensitivity of model results to the fixed coefficients will be presented in future papers.

In addition to the L–I–H transition, the model successfully reproduces a single-step sharp L–H transition, i.e. an L–H transition without passing through an I-phase, when the input heating power is well above the threshold or ramps up with a much faster rate. The L–I–H transition shown in figure 8 is obtained with a slow ramping rate of the heating power flux, Q. With a faster ramping rate, fewer dithering cycles appear. Furthermore, as the ratio of initial value U to V increases to a certain level, the L–H transition accomplishes in a single step, since the EF shear increases so quickly that it dominates over the contribution from the ZF shear in the Reynolds energy transfer term, $\alpha V^2 I$, which results in a net decay of the turbulence energy due to energy transfer into ZFs till the H-mode state is reached. In the H-mode, although the driving forces of turbulence—the pressure gradient—increase, the damping by the EF shear is so strong that it stops the recovery of the turbulence level.

In addition, the model is used to study H–L back transition. I-phases during the H–L back transition similar to that appearing during the L–H forward transition as well as the so-called 'hysteresis effect' in the transition power threshold are also successfully reproduced by this model. However, it is beyond the scope of this paper, and will be discussed in future papers.

5. Summary and discussions

In summary, a newly developed dual GPI system [55, 56] was used in the EAST 2012 campaign to study the L–I–H transition with input heating power close to or slightly above the L–H transition threshold. With the new dual GPI system, the time-resolved poloidal and radial plasma flows as well as the turbulence-driven Reynolds work at two well-separated locations can be obtained simultaneously by tracking the fast motion of turbulence structures in the plane perpendicular to the local magnetic field lines. It provides a new diagnostic for ZFs at the plasma edge [32, 57–59], thus allowing us to gain a deeper insight into the details of the transition dynamics. To facilitate the interpretation of experimental data, a new self-consistent 0D model, incorporating the time evolution of plasma pressure on both sides of the separatrix, turbulence intensity, EF shear, ZF shear, as well as parallel transport in the SOL, has been developed and successfully reproduced the L–I–H transition process with some features comparing favourably with the experimental observations. In addition, the state of the art of this research topic is reviewed briefly in the introduction.

A couple of interesting features of the L–I–H transition have been observed with the new dual GPI diagnostic:

- A slow increase in the poloidal flow and its shear at the plasma edge are observed tens of milliseconds prior to the I-phase. This slowly evolving poloidal flow may be associated with the EF.
- The fluctuation level appears to be strongly suppressed during the quiescent period in each dithering cycle. With reduced cross-field transport, the GPI emission intensity grows inside the separatrix and decays in the SOL, leading to a monotonic increase in the gradient near the separatrix. Then, the gradient collapses as it reaches a nearly constant threshold level, terminating the quiescent period.
- The flattening of the emission intensity profile is induced by a series of abrupt transient enhancement of turbulence at the plasma edge, with a fast growth phase typically less than 100 μs, which is much shorter than the quiescent period, typically of $\sim$500 μs, in each dithering cycle.
- The turbulent transient enhancement appears to originate from the vicinity of the separatrix with clear wave fronts propagating both outwards into the far SOL and inwards deeply into the plasma at a speed of 0.2 ± 0.1 km s^{-1} along the minor radius. This observation compares favourably with the recent 1D model, showing that the dithering cycle appears to be a nonlinear wave originating from the separatrix and propagating inwards [20, 21].
- An enhancement in the differential poloidal flows appears periodically in a radial range from the SOL up to 2 cm inside the separatrix just following the recovery of turbulent fluctuations in each dithering cycle, with a velocity up to -4 km s^{-1} in the electron diamagnetic direction inside the separatrix and up to 2 km s^{-1} in the ion diamagnetic direction outside the separatrix.
- The turbulence Reynolds stress and Reynolds work are directly measured with the GPI system in the experiments, showing a significant magnitude during the turbulent transient enhancement in a radial region slightly inside the separatrix, i.e. $r - r_{sep} = -2 \sim 0$ cm, which provides direct evidence of kinetic energy transfer from turbulence

to ZFs at the plasma edge. The Reynolds work has also been measured using Langmuir probe arrays in EAST [18] and recently in DIII-D [22] during the L–H transitions, in reasonable agreement with GPI measurements.

- Following a turbulent transient enhancement, the turbulence is quickly damped, possibly because its driving force—the pressure gradient—is weakened by the turbulent transient enhancement, which terminates the turbulent state and initiates a quiescent period. The differential poloidal flows decay subsequently (figure 5(*c*)), possibly due to the loss of turbulent drive. To a certain point, the turbulence level recovers, followed by the initiation of the next dithering cycle.
- Some small-amplitude oscillations in D_α emissions, appearing to be small-sized dithering cycles, at a frequency of several kHz, considerably higher than the repetition frequency of the normal dithering cycles, are frequently present prior to the I-phase or the L–H transition, acting like a transition precursor. Although with a smaller amplitude, these oscillations exhibit similar features of turbulence–flow interactions at the plasma edge.
- No GAM oscillation near its characteristic frequency is found in either GPI or reciprocating Langmuir probe data near the transition threshold conditions or in H-mode.
- In addition, no precursor MHD coherent modes prior to each dithering cycle like those frequently appearing prior to type-III ELMs are observed in either GPI or reciprocating Langmuir probe signals. This could be an important distinction between the dithering cycles and type-III ELMs.

The experimental results and the successful reproduction of the L–I–H transition by the 0D model suggest that the transition and the oscillatory behaviour during the I-phase could be induced by the synergistic effect of the two components of the sheared $m, n = 0\, \boldsymbol{E} \times \boldsymbol{B}$ flow, i.e. the ZF and the EF. As indicated by the model, two feedback loops exist at the plasma edge, associated with the two flow components, through which the fast energy transfer process and turbulence suppression at the transition are initiated. The experimental and modelling results presented in this paper strongly suggest the following physical picture of the L–I–H transition.

Turbulence suppression at the L–H transition could be induced by a reduction in turbulence energy input or by an enhancement in turbulence energy output. The turbulence energy input can be reduced due to the shear decorrelation mechanism through the reduction of the effective growth rate of the underlying instability of turbulence [36–38]. For the turbulence energy output, one important channel is transferring the kinetic energy downwards in the frequency domain from turbulence to low-frequency ZFs [31–33]. Another channel is scattering the turbulence spectral energy into the high-k dissipation regions [38]. Both the shear decorrelation and the energy transfer or scattering are controlled by the total $m, n = 0\, \boldsymbol{E} \times \boldsymbol{B}$ flow shear due to tilting and breaking of turbulence eddies [31]. For each limit cycle oscillation, the cycle starts with the suppression of the turbulence by the total $\boldsymbol{E} \times \boldsymbol{B}$ flow shear, leading to the subsequent damping of the ZFs, due to the loss of turbulent drive. To a certain point, the total $\boldsymbol{E} \times \boldsymbol{B}$ flow shear is insufficient to maintain turbulence suppression, so that the turbulence level recovers, which initiates the next dithering cycle. In addition, during the I-phase, the turbulence is periodically suppressed across the sheared region of the plasma edge, thus allowing the local pressure gradient and consequently the EF shear to build up progressively, which finally locks in the H-mode state.

In addition, our experiments suggest that the SOL physics may play an important role in the L–I–H transition dynamics. The SOL parameters set the boundary conditions for the dynamics inside the separatrix. One important new finding provided by the GPI data is the critical role of the evolution of pressure gradient near the separatrix for the LCO dynamics. The pressure gradient near the separatrix is proportional to the pressure difference between the inner side of the separatrix and the SOL. It is found in the experiments that a reduction in the SOL pressure significantly contributes to the increment of pressure gradient near the separatrix. This pressure gradient controls the EF, which has been shown to play an important role in the transition physics. An exponential decay in the divertor D_α emission as well as the GPI emission intensity in the SOL are observed during the quiescent period in each dithering cycle, on a time scale of the SOL particle confinement, $\tau_\parallel = L_\parallel/(M_\parallel C_s) \sim 500\,\mu$s. During the quiescent period, the particle and heat sources in the SOL are significantly reduced, since the cross-field transport is blocked by the flow shear at the plasma edge. The particle and heat in the SOL are therefore gradually exhausted through parallel transport, resulting in the exponential decay. When a turbulent transient enhancement occurs, the accumulated pressure inside the separatrix during the quiescent period is rapidly released by the strong turbulent ejection, which replenishes the SOL with fresh particles and heat, leading to a quick recovery of the SOL pressure.

Some critical issues still need to be addressed in future work. For example, recent experiments suggest that the ZFs may not play a dominant role in some types of LCOs [23–25]. On the other hand, supposing the zonal flows really play a significant role in the L–H transition, how to explain the transition power threshold scaling based on the zonal-flow-related microscopic dynamics? To address these questions, experiments need to develop new high-resolution edge diagnostic and combine several diagnostics to measure turbulence, density and temperature gradients, and all flow components in the main ion radial force balance equation simultaneously. Finally, the physics described by the simple L–I–H transition model should be captured by suitable fluid or gyrofluid edge-turbulence simulation codes. These could be used to gain deeper insights into the physics before turning to gyrokinetic-based large-scale simulations.

Acknowledgments

This work was supported by the National Magnetic Confinement Fusion Science Programme of China under Contract Nos 2011GB107001, 2011GB101000, 2013GB106000, 2013GB107003, 2012GB101000 and 2010GB104001, the National Natural Science Foundation of China under Contract Nos 11075181, 11021565, 10990212, 11105177 and the Sino Danish Center for Education and Research.

References

[1] Conway G.D.*et al* 2011 *Phys. Rev. Lett.* **106** 065001
[2] Itoh S.-I., Itoh K., Fukuyama A. and Miura Y. 1991 *Phys. Rev. Lett.* **67** 2485
[3] Ido T. *et al* 2000 *Plasma Phys. Control. Fusion* **42** A309
[4] Zohm H. *et al* 1994 *Phys. Rev. Lett.* **72** 222
[5] Cordey J.*et al* 1995 *Nucl. Fusion* **35** 505
[6] Jachmich S. *et al* 1998 *Plasma Phys. Control. Fusion* **40** 1105
[7] Colchin R.J. *et al* 2002 *Phys. Rev. Lett.* **88** 255002
[8] Colchin R.J. *et al* 2002 *Nucl. Fusion* **42** 1134
[9] Rudakov D.L. *et al* 2001 *Plasma Phys. Control. Fusion* **43** 559
[10] Wagner F. 2007 *Plasma Phys. Control. Fusion* **49** B1–B33
[11] Estrada T. *et al* 2010 *Europhys. Lett.* **92** 35001
[12] Zweben S.J. *et al* 2010 *Phys. Plasmas* **17** 102502
[13] Xu G.S. *et al* 2011 *Phys. Rev. Lett.* **107** 125001
[14] Estrada T. *et al* 2011 *Phys. Rev. Lett.* **107** 245004
[15] Sechrest Y. *et al* 2011 *Phys. Plasmas* **18** 012502
[16] Schmitz L. *et al* 2012 *Phys. Rev. Lett.* **108** 155002
[17] Zweben S.J. *et al* 2012 *Plasma Phys. Control. Fusion* **54** 025008
[18] Manz P. *et al* 2012 *Phys. Plasmas* **19** 072311
[19] Xu G.S. *et al* 2012 *Phys. Plasmas* **19** 122502
[20] Miki K. *et al* 2012 *Phys. Plasmas* **19** 092306
[21] Miki K. *et al* 2013 *Nucl. Fusion* **53** 073044
[22] Tynan G.R. *et al* 2013 *Nucl. Fusion* **53** 073053
[23] Hill D.N. and the DIII-D Team 2013 *Nucl. Fusion* **53** 104001
[24] Cheng J. *et al* 2013 *Phys. Rev. Lett.* **110** 265002
[25] Kobayashi T. *et al* 2013 *Phys. Rev. Lett.* **111** 035002
[26] Martin Y.R. *et al* 2008 *J. Phys.: Conf. Ser.* **123** 012033
[27] McKee G.R. *et al* 2009 *Nucl. Fusion* **49** 115016
[28] Yan Z. *et al* 2011 *Proc. 53rd APS Meeting of Plasma Physics (Salt Lake City, UT, 14–18 November, 2011)* GO4.006 http://meetings.aps.org/Meeting/DPP11/Session/GO4.6
[29] Xu M. *et al* 2012 *Phys. Rev. Lett.* **108** 245001
[30] Kim E.-J. and Diamond P.H. 2003 *Phys. Rev. Lett.* **90** 185006
[31] Diamond P.H. *et al* 2005 *Plasma Phys. Control. Fusion* **47** R35
[32] Fujisawa A. 2009 *Nucl. Fusion* **49** 013001
[33] Diamond P.H. *et al* 1994 *Phys. Rev. Lett.* **72** 2565
[34] Shaing K.C. and Crume E.C. 1989 *Phys. Rev. Lett.* **63** 2369
[35] Chang C.S., Kue S. and Weitzner H. 2002 *Phys. Plasmas* **9** 3884
[36] Biglari H., Diamond P.H. and Terry P.W. 1990 *Phys. Fluids* B **2** 1
[37] Terry P.W. 2000 *Rev. Mod. Phys.* **72** 109
[38] Gürcan Ö.D. *et al* 2012 *Phys. Rev. Lett.* **109** 155006
[39] Smolyakov A.I. and Diamond P.H. 1999 *Phys. Plasmas* **6** 4410
[40] Wolfrum E. 2012 *Plasma Phys. Control. Fusion* **54** 124002
[41] Sauter P. *et al* 2012 *Nucl. Fusion* **52** 012001
[42] Ryter F. *et al* 2009 *Nucl. Fusion* **49** 062003
[43] Ryter F. *et al* 2012 *Nucl. Fusion* **52** 114014
[44] Ma Y. *et al* 2012 *Nucl. Fusion* **52** 023010
[45] Meyer H. *et al* 2011 *Nucl. Fusion* **51** 113011
[46] Gohil P. *et al* 2009 *Nucl. Fusion* **49** 115004
[47] Gohil P. *et al* 2010 *Nucl. Fusion* **50** 064011
[48] Gohil P. *et al* 2011 *Nucl. Fusion* **51** 103020
[49] Maingi R. *et al* 2010 *Nucl. Fusion* **50** 064010
[50] Kaye S.M. *et al* 2011 *Nucl. Fusion* **51** 113019
[51] Xu G.S. *et al* 2011 *Nucl. Fusion* **51** 072001
[52] Estrada T. *et al* 2012 *Plasma Phys. Control. Fusion* **54** 124024
[53] Estrada T. *et al* 2011 *Nucl. Fusion* **51** 032001
[54] Li J. and Wan B. 2011 *Nucl. Fusion* **51** 094007
[55] Liu S.C. *et al* 2012 *Rev. Sci. Instrum.* **83** 123506
[56] Fedorczak N. *et al* 2012 *Phys. Plasmas* **19** 122302
[57] Xu G.S. *et al* 2003 *Phys. Rev. Lett.* **91** 125001
[58] Liu A.D. *et al* 2009 *Phys. Rev. Lett.* **103** 095002
[59] Fujisawa A. *et al* 2004 *Phys. Rev. Lett.* **93** 165002
[60] Whyte D.G. *et al* 2010 *Nucl. Fusion* **50** 105005
[61] Ryter F. *et al* 1998 *Plasma Phys. Control. Fusion* **40** 725
[62] Maqueda R.J. *et al* 2003 *Rev. Sci. Instrum.* **74** 2020
[63] Yan N. *et al* 2011 *Plasma Sci. Technol.* **13** 410
[64] Stotler D. *et al* 2003 *J. Nucl. Mater.* **313–316** 1066
[65] Stotler D. *et al* 2007 *J. Nucl. Mater.* **363–365** 686
[66] Munsat T. and Zweben S.J. 2006 *Rev. Sci. Instrum.* **77** 103501
[67] Terry J. *et al* 2005 *J. Nucl. Mater.* **337–339** 322
[68] McKee G.R. *et al* 2004 *Rev. Sci. Instrum.* **75** 3490
[69] Holland C. *et al* 2004 *Rev. Sci. Instrum.* **75** 4278
[70] Zweben S.J. *et al* 2004 *Nucl. Fusion* **44** 134
[71] Zhang W. *et al* 2010 *Rev. Sci. Instrum.* **81** 113501
[72] Sánchez E. *et al* 2005 *J. Nucl. Mater.* **337–339** 296
[73] Xu G.S. *et al* 2009 *Nucl. Fusion* **49** 092002
[74] Xu G.S. *et al* 2011 *Plasma Sci. Technol.* **13** 397
[75] Itoh K. and Itoh S.-I. 1996 *Plasma Phys. Control. Fusion* **38** 1
[76] Rosenbluth M.N. and Hinton F.L. 1998 *Phys. Rev. Lett.* **80** 724
[77] Groebner R.J. *et al* 1990 *Phys. Rev. Lett.* **64** 3015
[78] Zweben S.J. *et al* 2007 *Plasma Phys. Control. Fusion* **49** S1
[79] Wagner F. *et al* 1984 *Phys. Rev. Lett.* **53** 1453